Numerical investigation of the near-injector flow of a CH_4-O_2 flame using finite-rate chemistry modeling

BARI, ITALY | 18 – 21 MAY 2026

Jan van Schyndel[1,3], **Edoardo La Cava** [2], **Justin Hardi**[1], **Jan Deeken**[1,4]
[1] *German Aerospace Center (DLR), Hardthausen, Germany, Email: jan.vanschyndel@dlr.de*
[2] *Department of Mechanical and Aerospace Engineering - DIMA, Sapienza – Università di Roma, Rom, Italy*
[3] *RWTH Aachen University, Aachen, Germany*
[4] *Institut für Strahlantriebe und Turbomaschinen, RWTH Aachen University, Aachen, Germany*

KEYWORDS: methane, combustion, CFD, Finite rate, flame anchoring

ABSTRACT:

A stable combustion is crucial for the operation of a rocket engine. One of the major factors for the stability of the combustion is the flame anchoring at the injector post. Unfortunately, the understanding of the underlying physic regarding the flame anchoring is still limited and the influencing factors of the injector design and fuel properties are insufficient understood for reliable a priori predictions.

To address this gap this, work numerically investigates flame anchoring and near-injector flow physics for a recessed, non-tapered shear-coaxial CH_4-O_2 element under high-pressure, cryogenic inlet conditions representative of rocket engines. To allow a wide range of parameters to be investigated, the configuration is reduced to a 2D axisymmetric setup. 2D CFD simulations where performed using the DLR TAU-Code using a finite rate combustion model, the SRK-real-gas -equation and two-equation turbulence model.

The results show that methane injection temperature and mixture ratio exert the strongest impact on anchoring behavior. Very cold fuel promotes unsteadiness and localized lift-off, whereas sufficiently hot fuel can lead to full flame detachment. Increasing the mixture ratio shifts the anchoring position upstream toward the LOX post. A larger LOX-post thickness consistently moves the flame core downstream by enlarging the recirculation region.

1. INTRODUCTION

Methane–oxygen propulsion is gaining attention for reusable launch systems and in-space applications. It offers favorable storage properties, system-level benefits, and the potential for lower lifecycle costs. Accurate prediction of flame stabilization and anchoring is essential for high-pressure rocket combustion. Small shifts in flame attachment strongly affect engine stability, injector durability, and thermal loads at the combustor inlet. These effects influence the entire engine cycle including turbopump behavior. Predicting flame anchoring and stabilization behavior remains challenging, as high-pressure methane–oxygen combustion involves strong real-gas effects, steep density gradients, and complex turbulence–chemistry interactions. These challenges are further amplified in methane–oxygen systems compared to hydrogen, as methane shows slower chemical reactivity, exhibits narrower extinction limits, and is more sensitive to mixing and thermal conditions. As a result, reliable modeling of flame anchoring is substantially more difficult for methane.

This work numerically investigates flame anchoring and near-injector flow physics for a recessed, non-tapered shear-coaxial CH_4-O_2 element under high-pressure, cryogenic inlet conditions representative of rocket engines. Although, this injector type is widely adopted in modern propulsion systems for its effective atomization and mixing performance (largely rooted in hydrogen injector heritage), it shows a more complex flame-stabilization behavior when operated with methane. Since classical flamelet models fail to capture the relevant anchoring physics, a finite-rate chemistry formulation is employed, increasing computational cost.

Simulations are performed using the DLR TAU solver with the Zhukov–Kong high-pressure methane mechanism. Real-gas effects are modeled using the Soave–Redlich–Kwong equation of state, and turbulence is described by a two-equation RANS model with appropriate near-wall treatment. To enable broader parameter study at manageable cost, the configuration is reduced to a 2D axisymmetric setup. The subsequent parametric study examines the influence of methane and oxygen injection temperatures, chamber pressure, mixture ratio, LOX-post thickness, and injector-tip thermal condition. The evaluation is based on OH mass-fraction fields, radial density and temperature profiles, and metrics describing flame attachment and the dominant swirl center.

The results show that methane injection temperature and mixture ratio exert the strongest impact on anchoring behavior. Very cold fuel promotes unsteadiness and localized lift-off, whereas sufficiently hot fuel can lead to full flame detachment. Increasing the mixture ratio—at either fixed total mass flow or fixed LOX mass flow—thickens the reaction zone and shifts the anchoring position upstream toward the LOX post. A larger LOX-post thickness consistently moves the flame core downstream by enlarging the recirculation region. In contrast, oxygen injection temperature within practical limits and the post-tip wall temperature have only minor influence on overall flame structure. Higher chamber pressure strengthens flame at-

tachment and reduces diffusion length scales. These findings represent the initial stage of a broader investigation aimed at developing a more comprehensive understanding of methane-oxygen flame anchoring under realistic rocket-engine conditions. Ongoing work extends the analysis towards three-dimensional configurations, transient behavior, more complex geometries and multi-injector interactions.

2. Numerical Setup and Physical Modeling

All numerical simulations presented here were performed using the DLR TAU-code [1] [2]. The DLR TAU-code is a density-based finite-volume solver with second-order accuracy solving the compressible Navier-Stokes equations. In the past the DLR TAU-code has been used to investigate a wide range of different flow phenomena, including steady and unsteady flows, covering velocities from subsonic to supersonic, nonreactive and reactive flows with different combustion models [3] [4]. In the present work an edge-based dual-cell approach based on a vertex-centered scheme is used. An explicit upwind solver with the standard MAPS$^+$ scheme is employed [5]. Viscous fluxes are evaluated using the full gradient-based formulation and gradients are reconstructed using a least-squares method. Turbulence is modeled using the Reynolds-averaged Navier-Stokes (RANS) approach with the two-equation Menter-Rumsay k-ϵ turbulence model [6]. To enhance convergence behavior, residual smoothing algorithms and local time-stepping are applied. The converged solution is obtained using a Courant-Friedrichs-Lewy (CFL) number of 0.1. Turbulent mass-diffusion fluxes and enthalpy fluxes are modeled using constant turbulent Schmidt and Prandtl numbers, of $\mathrm{Sc_{tr}} = 0.7$ and $\mathrm{Pr_{tr}} = 0.9$, respectively. All simulations are initialized using the solution of a flamelet simulation to establish the main flow topology (recirculation zones, shear layers and scalar gradients) at low computational cost [7]. Afterwards the computation is transitioned to a finite-rate chemistry simulation and again advanced to convergence. During the handover, temperature and major species fields are mapped from the flamelet space to the native species used by FRC. To avoid spurious transients, the CFL is temporarily reduced, then relaxed once the stiff kinetics stabilize.

WIthin the finite rate simulations the chemical kinetics is modeled using a skeletal mechanism for high-pressure methane-oxygen combustion, originally developed by Zhukov and Kong at the DLR Institute of Space Propulsion [8]. In its original form, the mechanism comprises 23 species and 51 reactions. For the pure methane-oxygen configuration considered here, the two neutral diluent species N_2 and Ar are excluded, yielding a reduced mechanism of 21 species and 49 reactions. To be able to correctly describe the cryogenic mixture effects, the Soave-Redlich-Kwong (SRK) cubic equation of state is applied to the injected propellants. For non-premixed combustion in coaxial injectors, real-gas effects are mainly confined to the cold pure oxidizer and fuel streams near the injector inlets. Combustion products, by contrast, form exclusively in the hot gas region, where temperatures and pressures are such that ideal-gas approximations remain valid. It is therefore sufficient to apply real-gas thermodynamic treatment only to the injected species, as demonstrated by Horchler et al. [9].

2.1 Finite-Rate Chemistry Modeling

Finite-rate chemistry modeling accounts for the actual rate of chemical reactions in each cell of the fluid doaim according to the local composition and thermodynamic properties, rather than assuming an instantaneous equilibrium. The approach solves transport equations for each individual species mass fractions along with source terms that depend on reaction rates:

$$\frac{\partial(\rho Y_k)}{\partial t} + \frac{\partial}{\partial x_i}\left(\rho u_i Y_k\right) = -\frac{\partial}{\partial x_i}\left(\rho V_{i,k} Y_k\right) + \dot{\omega}_k. \quad (1)$$

The index $i = 1, 2, 3$ follows Einstein's tensor notation with numerical indexing of the spatial coordinate directions. In this context, with k=1,... N_s and N_s representing the number of species in the kinetic mechanism, while Y_k and $\dot{\omega}_k$ denote the mass fraction and the net formation rate of species k, respectively. $V_{i,k}$ are the diffusion velocities of species k in direction i and are evaluated by Fick's law.

Using the the law of mass action, for reversible reactions, the net reaction rate of the production of species can be computed as:

$$\dot{\omega}_k = \sum_{j=1}^{N_r}\left(\nu''_{k,j} - \nu'_{k,j}\right)\left[k_{f,j}\prod_{k=1}^{N_s}\left(\frac{\rho Y_k}{\mathcal{M}_k}\right)^{\nu'_{k,j}} - k_{b,j}\prod_{k=1}^{N_s}\left(\frac{\rho Y_k}{\mathcal{M}_k}\right)^{\nu''_{k,j}}\right]. \quad (2)$$

Here $\nu'_{k,j}$ and $\nu''_{k,j}$ are the molecular stoichiometric coefficients of species k in forward and backward reactions, respectively, $k_{f,j}$ and $k_{b,j}$ are the forward and backward rates of reactions j, respectively. These rates depend on temperature and are computed from the Arrhenius law for the forward rates:

$$k_{f,j} = A_{f,j} T^{\beta_j} \exp\left(-\frac{E_{f,j}}{\mathcal{R}T}\right), \quad (3)$$

and using the equilibrium constants for backward rates:

$$k_{b,j} = \frac{k_{f,j}}{\left(\frac{p_{\mathrm{ref}}}{\mathcal{R}T}\right)^{\sum_{k=1}^{N_s}\left(\nu''_{k,j}-\nu'_{k,j}\right)} \exp\left(\frac{\Delta S^0_j}{\mathcal{R}} - \frac{\Delta H^0_j}{\mathcal{R}T}\right)}. \quad (4)$$

Where $A_{f,j}$, β_j and $E_{f,j}$ are the pre-exponential factor, the temperature exponent and the forward activation energies of reactions j, respectively. ΔS^0_j and ΔH^0_j refer to the enthalpy and the entropy changes occurring when passing from reactants to products, while p_{ref} = 1 atm.

3. Test Case

The injector configuration examined in this study correlates to a recessed, non-tapered shear coaxial injector. In this arrangement, the oxidizer is supplied through a central tube, while the fuel flows through a surrounding concentric annulus. The design follows the generic test case from the REST HF-10 [10] workshop and is representative for commonly employed injectors in liquid rocket propulsion systems. The aim is to study a simplified yet practically relevant configuration, which captures key features of shear-driven mixing while avoiding geometric complexity that might obscure fundamental behavior. The terms *non-tapered* and *recessed* refer, respectively, to the constant cross-sectional area of the injector channels and the axial setback of the inner post relative to the outer annular exit. The computational domain is modeled as a two-dimensional, axisymmetric geometry, as illustrated in Fig. 1. This approach leverages the inherent symmetry of the problem, significantly reducing the computational cost without compromising the accuracy of the results [11]. Within this domain, field-sampling abscissae are placed at discrete axial locations downstream of the LOX post to capture the evolution of the near-injector flow field. The geometric parameters of the computational domain are summarized in Table 1. It has been demonstrated that the selected axial lengths of the LOX and CH_4 inlet channels are sufficient to allow adequate development of the turbulent velocity profiles at the LOX post exit [7]. While axial lengths are kept constant across all simulations, the effect of varying the LOX post tip thickness (h) is also investigated, which leads to adjustments in the corresponding radii defined in Table 1.

The boundary conditions applied in all simulations are illustrated in Figure 2. The LOX and CH_4 inlets are prescribed as reservoir-pressure inflow boundaries, while the outlet is modeled as an exit-pressure outflow. All domain walls are modeled as adiabatic viscous boundaries, except for the LOX post tip. This surface is treated as a viscous wall with a thermal reservoir boundary condition, where a one-dimensional approximation of the heat transfer is assumed: $q = \lambda/w\,(T_w - T_{res})$. The wall is assumed to be 1-mm-thick, with thermal conductivity representative of CuCrZr alloy properties near 500 K and internal (reservoir) temperature nominally fixed to 475 K. The selected boundary conditions are based on physical considerations and previous simulation results [7]. The injection conditions prescribed for the reference case are intended to be representative of established numerical benchmarks and characteristic operating points for methane/oxygen combustion chambers [12] [13] [14] [15] [16]. For the reference case, the chamber pressure is set to p_c = 6 MPa with methane and oxygen mass flow rates of 0.136 kg/s and 0.460 kg/s (O/F = 3.4), respectively, at inlet temperatures of 249 K and 107 K. The computational domain is discretized using a fully structured axisymmetric mesh. Detailed mesh specifications are available in [17].

L_{RC} [mm]	L_{O_2} [mm]	L_{CH_4} [mm]	$R^{int}_{O_2}$ [mm]	$R^{ext}_{O_2}$ [mm]	R_{CH_4} [mm]	h [mm]
20	100	20	3.15	3.60	4.10	0.45

Table 1: Reference domain dimensions.

4. Investigation on Flame Anchoring

The main parameter controlling shear-coaxial elements performance is the axial fuel-to-oxidizer momentum ratio:

$$J = \frac{(\rho u^2)_{\text{fuel}}}{(\rho u^2)_{\text{ox}}} = \frac{(\rho A^2)_{\text{ox}}}{(\text{O/F})^2\,(\rho A^2)_{\text{fuel}}} \tag{5}$$

The latter directly connects the momentum ratio to the geometry of the injection element and includes the effect of the propellants mixture ratio. Larger momentum ratios support more rapid atomization, leading to a more efficient mixing. Proper momentum ratio selection ensures adequate mixing time and contact area between the propellants before they exit the shear-driven mixing zone: too low a ratio may result in poor mixing and incomplete combustion, while too high a ratio can cause excessive pressure drop or unstable flow patterns. Figure 3 compares the measured axial flame attachment locations across the different studies conducted during the parametric campaign to identify the primary injection parameters controlling flame lift-off. Shading within each dataset indicates the direction of parameter increase for the investigated variable. While J parameter variations control flame anchoring position, the mechanism through which these variations are achieved substantially alters the stabilization behavior. Regardless of the specific implementation method, a progressive increase in momentum flux ratio consistently leads to increased flame lift-off distance. This behavior is attributed to the higher momentum of the methane stream compared to the denser oxygen, causing a downstream displacement of the swirl center. Results indicate that methane injection temperature and mixture ratio are the dominant parameters governing flame anchoring behavior. While a more comprehensive examination has been performed [17], the present work focuses exclusively on these two variables. For all fluids involved, a velocity ratio (VR = u_{CH_4}/u_{O_2}) and a density ratio (DR = ρ_{O_2}/ρ_{CH_4}) can be defined. A velocity ratio much larger than unity is desired: in such cases, the near field of the coaxial jet is characterized by the appearance of hydrodynamic instability which grows, forming three-dimensional vortices, convected downstream by the mean flow. A direct consequence of this instability is thus the formation of interface corrugations which increase the contact area between both streams. This plays a primary role in the overall mixing and entrainment, and consequently heat-release due to increased wrinkling of the resulting diffusion flame.

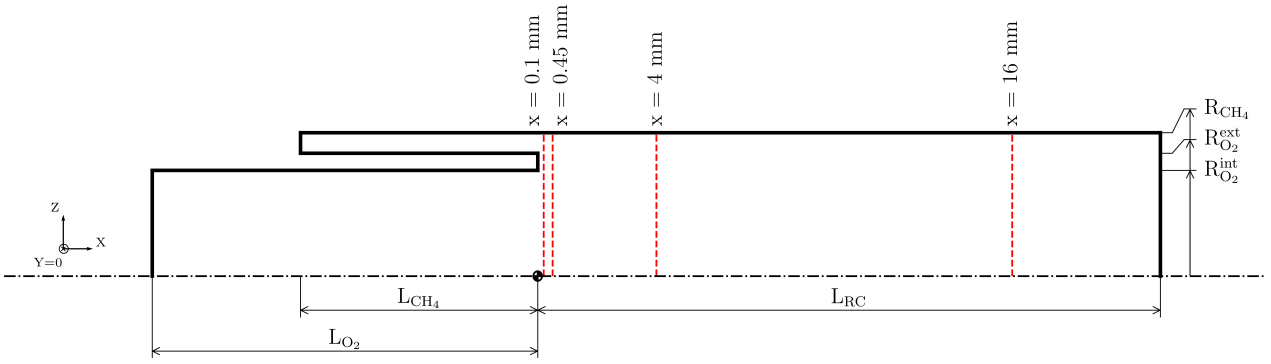

Figure 1: Schematic representation of the computational domain and field sampling abscissae.

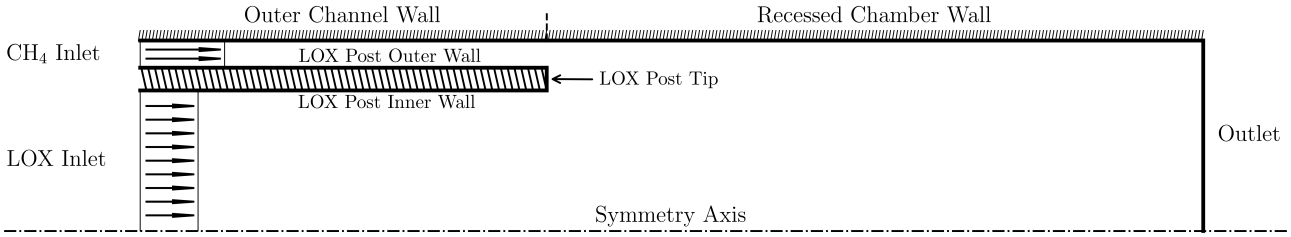

Figure 2: Schematic representation of the prescribed boundary conditions.

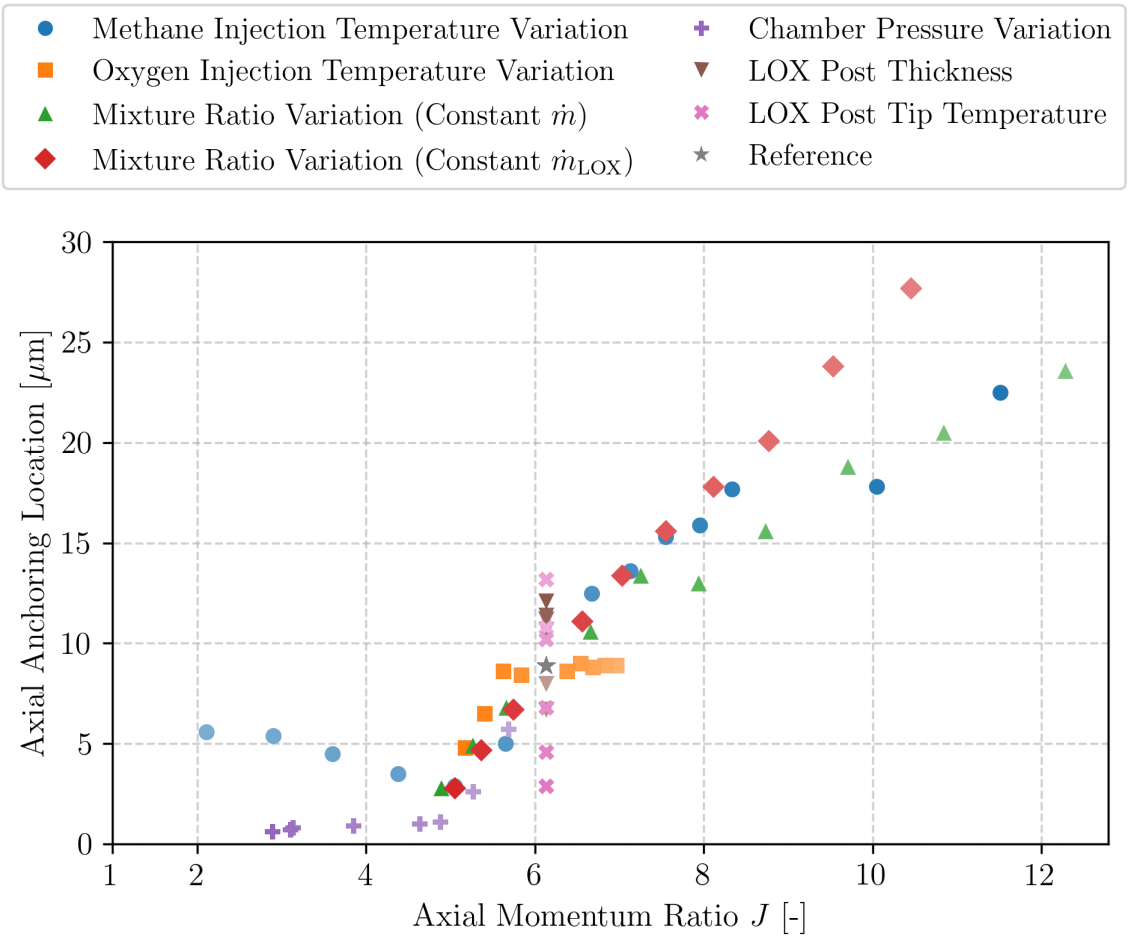

Figure 3: Variation of flame axial anchoring location with axial momentum ratio across all investigated parametric conditions and regimes. Shading indicates the direction of parameter increase.

4.1 Effect of Methane Injection Temperature Variations

Tab. 2 provides an overview of input parameters and non-dimensional characteristic values analyzed in this study. The investigated Methane injection temperature ranges from T_{CH_4} = 100 K to 450 K to represent operating conditions of a main combustion chamber injectors and to explicitly examine methane injection in both supercritical and liquid-like phases. Fig. 4 shows OH mass fraction contours in the near-injector region for selected cases. Among the intermediate species formed during combustion, OH is a short-lived intermediate species that forms predominantly in high-temperature regions where reaction rates are highest. Since it exists solely within the combustion zone and recombines rapidly, it serves as a reliable indicator of the flame front and as a marker of the chemical reaction zone. Experimentally, the OH radical is used to visualize flames in combustion chambers: narrow band-pass optical filters isolate OH* ultraviolet chemiluminescence (310 nm), enabling non-intrusive imaging of the flame structure and anchoring region through chamber windows even under high-pressure conditions [18]. Its spatial distribution offers therefore valuable insights into the flame's location, structure and anchoring behavior under varying operating conditions. At cryogenic injection temperatures (Fig. 4a - 4c), the steady RANS solutions exhibit pronounced oscillations that persist, indicating inherently unsteady behavior in this regime. These oscillations diminish as the injection temperature increases and are no longer observed at approximately T_{CH_4} = 180 K.

T_{CH_4} [K]	VR [-]	DR [-]	J [-]
100	1.80	2.40	1.36
120	1.92	2.55	1.45
140	2.10	2.79	1.58
160	2.36	3.14	1.78
180	2.81	3.73	2.11
200	3.85	5.11	2.90
210	4.77	6.34	3.60
220	5.81	7.71	4.38
230	6.71	8.90	5.05
240	7.50	9.95	5.65
249	8.14	10.80	6.13
260	8.86	11.76	6.67
270	9.46	12.56	7.13
280	10.02	13.30	7.55
290	10.55	14.01	7.95
300	11.06	14.68	8.33
350	13.35	17.72	10.05
400	15.29	20.31	11.51
450	17.02	22.61	12.81

Table 2: Non-dimensional parameters at increasing methane injection temperature ($\dot{m}_{LOX}$ = 0.460 kg/s, $\dot{m}_{CH_4}$ = 0.136 kg/s, T_{LOX} = 107 K, p_c = 6 MPa).

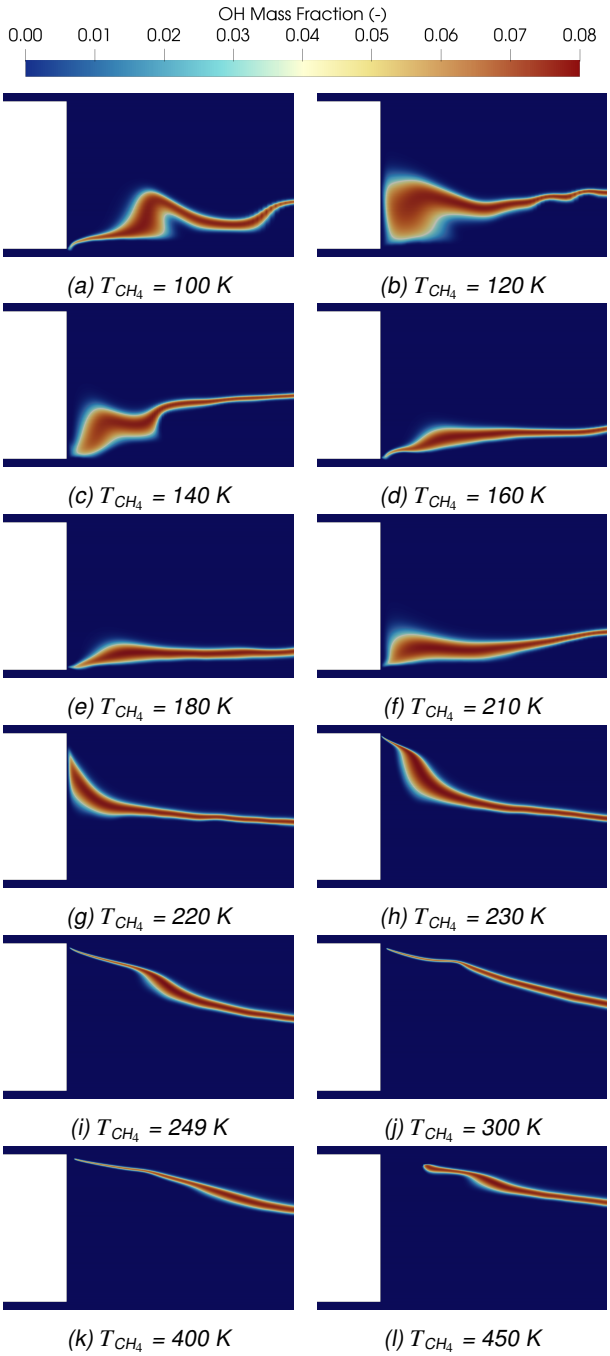

Figure 4: Near-injector region OH mass fraction contours for different methane injection temperatures.

To assess whether the observed unsteadiness is physical, unsteady RANS simulations (URANS) were performed. Each URANS case was initialized from the corresponding steady RANS field and then advanced using a Jameson-type [19] dual time stepping approach with a physical time step of $\Delta t = 5.0 \times 10^{-8}$ s for long enough to eliminate possible transient effects in the model transition. This timestep ensures that the local CFL number remains below unity on the smallest near-post cells and follows temporal-resolution guidance reported for LOX/CH_4 flames in the literature [12]. The instantaneous OH mass fraction contours shown in Fig. 5 confirm what was initially observed in RANS simulations: the flame undergoes strong oscillations

and exhibits localized lift-off downstream of the LOX post. Despite these dynamic oscillations, examination of the time-averaged contours reveals that the flame remains anchored at the LOX post tip [17]. Upon increasing the injection temperature from T_{CH_4} = 210 K to 230 K, the flame attachment point shifts drastically from the methane side toward the oxygen side of the post tip. Concurrently, the downstream core reaction zone becomes progressively thinner until, at T_{CH_4} = 450 K, the flame completely detaches from the LOX post. Varying the fuel injection temperature modifies the injected fuel density and, at fixed mass flow rate, the injection velocity. This parametric variation helps identify two practical limits: (i) a low-velocity threshold below which the recirculation zones behind the LOX-post tip are too weak to anchor the flame, and (ii) a high-velocity regime in which elevated strain rates suppress flame attachment at the LOX-Post tip.

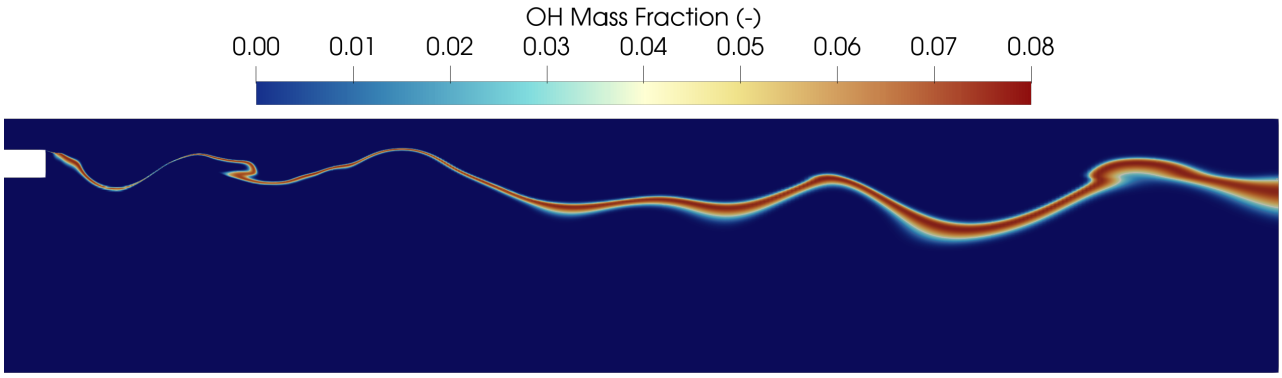

(a) $t = \tau + 0.5$ ms

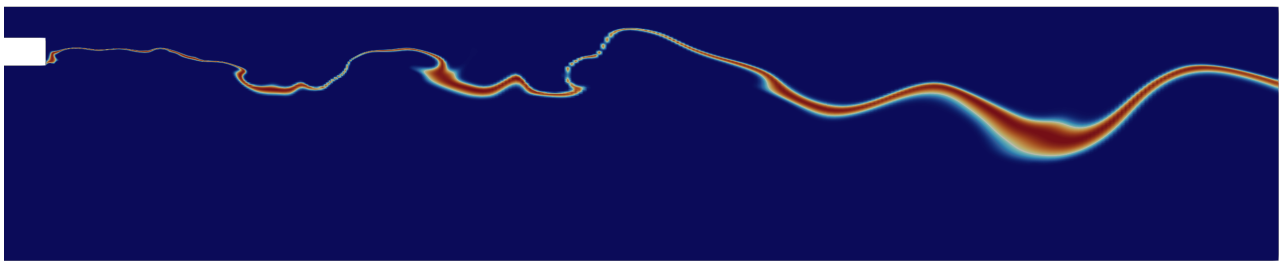

(b) $t = \tau + 0.7$ ms

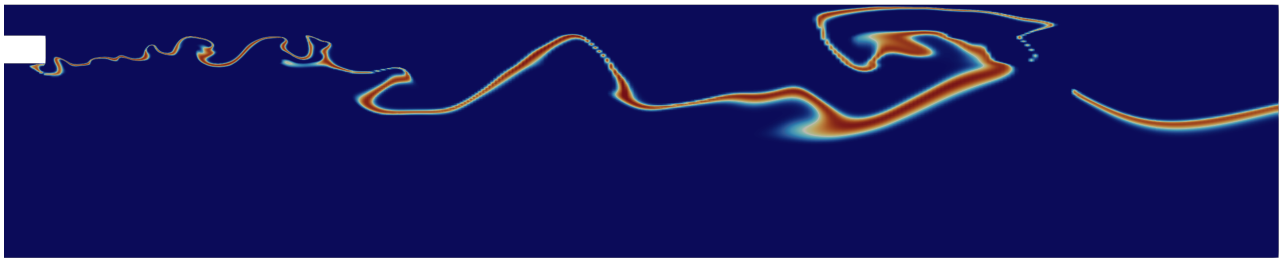

(c) $t = \tau + 0.8$ ms

Figure 5: Instantaneous OH mass fraction contours at T_{CH_4} = 100 K.

O/F [-]	$\dot{m}_{LOX}$ [kg/s]	$\dot{m}_{CH_4}$ [kg/s]	VR [-]	DR [-]	J [-]
2.0	0.397	0.199	9.58	7.48	12.28
2.2	0.410	0.186	9.31	8.00	10.84
2.4	0.421	0.175	9.09	8.52	9.70
2.6	0.430	0.166	8.86	9.00	8.73
2.8	0.439	0.157	8.68	9.48	7.94
3.0	0.447	0.149	8.50	9.95	7.25
3.2	0.454	0.142	8.32	10.40	6.66
3.4	0.460	0.136	8.14	10.80	6.13
3.6	0.466	0.130	7.96	11.19	5.66
3.8	0.472	0.124	7.80	11.58	5.26
4.0	0.477	0.119	7.64	11.94	4.89

Table 3: Characteristic non-dimensional parameters and mass flow rates at increasing mixture ratio for constant total mass flow rate ($T_{LOX} = 107\,\mathrm{K}$, $T_{CH_4} = 249\,\mathrm{K}$, $p_c = 6\,\mathrm{MPa}$).

O/F [-]	$\dot{m}_{CH_4}$ [kg/s]	$\dot{m}$ [kg/s]	VR [-]	DR [-]	J [-]
2.0	0.230	0.690	8.16	6.37	10.45
2.2	0.209	0.669	8.19	7.03	9.53
2.4	0.192	0.652	8.22	7.70	8.77
2.6	0.177	0.637	8.23	8.36	8.11
2.8	0.164	0.624	8.25	9.02	7.55
3.0	0.153	0.613	8.24	9.65	7.03
3.2	0.144	0.604	8.20	10.25	6.56
3.4	0.136	0.595	8.14	10.80	6.13
3.6	0.128	0.588	8.06	11.33	5.74
3.8	0.121	0.581	7.96	11.81	5.36
4.0	0.115	0.575	7.88	12.31	5.05

Table 4: Characteristic non-dimensional parameters and mass flow rates at increasing mixture ratio for constant oxidizer mass flow rate $\dot{m}_{LOX} = 0.460\,\mathrm{kg/s}$ ($T_{LOX} = 107\,\mathrm{K}$, $T_{CH_4} = 249\,\mathrm{K}$, $p_c = 6\,\mathrm{MPa}$).

4.2 Effect of Mixture Ratio Variations

Two distinct operational conditions are considered in this study: constant overall mass flow rate and constant LOX mass flow rate. In both cases, the mixture ratio is varied from O/F = 2.0 to 4.0 in steps of 0.2. The corresponding input parameters and non-dimensional characteristic values are summarized in Tab. 3 and Tab. 4. This type of parametric study is conducted to identify potential instability regimes within the operating envelope. For instance, experimental investigations at the European Research and Technology Test Facility P8 for cryogenic rocket engine testing at DLR Lampoldshausen revealed instability phenomena in specific operating regimes for both research combustion chambers BKN and BKD [20]. Fig. 6 displays OH mass fraction contours in the near-injector region for selected cases under constant overall mass flow rate and constant LOX mass flow rate, respectively. Analysis of these contours indicates that, in both configurations, the flame initially undergoes stretching before transitioning to a thickening phase, concurrent with upstream migration of the flame head toward the injector tip. In particular, in the constant overall mass flow rate case, this phenomenon occurs because doubling the mixture ratio while maintaining constant overall mass flow rate results in a 20% increase in LOX mass flow rate and a corresponding 67% decrease in the less dense methane mass flow rate. This differential change causes the velocity ratio and momentum ratio to progressively decrease, creating an interaction zone that worsens the dense core breakup and reduces mixing. At high ROF, the swirl pattern in the mixture region downstream of the LOX post shifts closer to the injector tip, producing a thicker flame structure. The same dynamics are observed in the constant LOX mass flow rate case, where the progressive reduction in methane mass flow rate drives an analogous evolution of the flame structure.

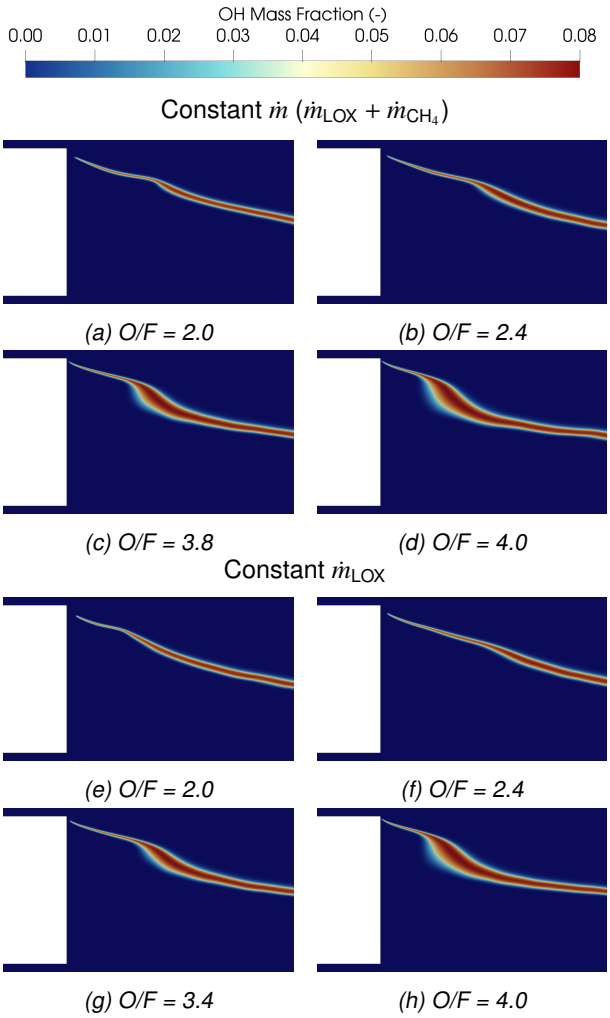

Figure 6: Near-injector region OH mass fraction contours for selected mixture ratios under constant overall mass flow rate (top) and constant LOX mass flow rate (bottom).

5. Conclusions

This research presented a numerical investigation of flame anchoring in a simplified, recessed, non-tapered shear-coaxial CH_4/O_2 injector operating under cryogenic, high-pressure, rocket-relevant conditions. The computational framework employed the DLR TAU solver with a finite-rate chemistry model, real-fluid thermodynamics for the injected propellants and a two-equation RANS turbulence closure. The principal outcomes of the two parametric investigations presented in this work can be summarized as follows. Increasing methane injection temperature enhances the outer annular-jet momentum, progressively thinning the reaction zone and shifting the flame toward the fuel side, until complete flame detachment occurs. Conversely, cryogenic fuel injection promotes flow unsteadiness and localized flame lift-off. Increasing the mixture ratio, whether at constant overall mass flow rate or constant LOX mass flow rate, thickens the flame and drives the anchoring point upstream toward the injector tip.

ACKNOWLEDGMENTS

The author is grateful to Edoardo La Cava for his excellent work during his thesis at DLR Lampoldshausen. Financial support from the German Aerospace Center (DLR) through project NOVASIM (Numerical Tool Optimisation and Verification for the Analysis of Propulsion Systems and Investigation of Methane Combustion), along with access to computational resources on the CARO cluster, is gratefully acknowledged. Special thanks are extended to all colleagues at DLR Göttingen for their continuous support and constructive discussions.

5 REFERENCES

[1] D. Schwamborn *et al.*, “Development of the TAU-code for aerospace applications,” 2008.

[2] D. Schwamborn *et al.*, “The DLR TAU-code: Recent applications in research and industry,” 2006.

[3] S. Karl, “Numerical investigation of a generic scramjet configuration,” 2011.

[4] D. Schneider *et al.*, “Numerical model for nozzle flow application under liquid oxygen/methane hot-flow conditions,” 2018.

[5] C.-C. Rossow, “Extension of a compressible code toward the incompressible limit,” 2003.

[6] F. Menter and C. Rumsey, “Assessment of two-equation turbulence models for transonic flows,” 1994.

[7] L. Klink, “Numerische untersuchung des einflusses von randbedingungen auf die injektornahe CH4-O2 flamme in raketenbrennkammern,” 2023.

[8] V. P. Zhukov and A. Kong, “A compact reaction mechanism of methane oxidation at high pressures,” 2018.

[9] T. Horchler *et al.*, “Recent developments in the DLR TAU code for combustion chamber modeling,” 2019.

[10] T. Schmitt, R. Kaess, *et al.*, “Rest hf-10 test case: Synthesis of the contributions for the simulation of excited methane flames under real gas conditions,” in *Proceedings of the 9th European Conference for Aeronautics and Space Sciences (EUCASS)*, 2022.

[11] R. Keller and P. M. Gerlinger, “Numerical simulations of a single injector gaseous methane rocket combustion chamber,” 2016.

[12] T. Horchler *et al.*, “Analysis of detailed-chemistry schemes for the numerical simulation of supercritical LOx/CH4 flames,” 2023.

[13] S. Fechter *et al.*, “Generic test case to understand cryogenic methane combustion dynamics,” 2020.

[14] J. van Schyndel *et al.*, “Numerical investigation of supercritical LOx/methane cryogenic combustion in a rocket combustion chamber,” 2025.

[15] J. C. Deeken *et al.*, “LUMEN demonstrator - project overview,” 2021.

[16] J. van Schyndel *et al.*, “Overview of the CFD modelling activities regarding the BKN combustion chamber at DLR Lampoldshausen,” 2024.

[17] E. La Cava, “Numerical investigation of boundary conditions on the near-injector flow of a CH4-O2 flame using finite-rate chemistry modeling,” 2025.

[18] J. Martin *et al.*, “Flame characteristics and response of a high-pressure LOX/CNG rocket combustor with large optical access,” 2022.

[19] A. Jameson, “Time dependent calculations using multigrid, with applications to unsteady flows past airfoils and wings,” 1991.

[20] J. Martin *et al.*, “Influence of injector and chamber geometry on the thermoacoustic behaviour in proximity to the stability boundary of LOX/CH4 rocket combustors,” 2025.